Experimental and numerical study of an elevated pool fire scenario in a confined and mechanically ventilated compartment

Samuel Vaux, Emeline Georges, Hugues Pretrel

To cite this version:

Samuel Vaux, Emeline Georges, Hugues Pretrel. Experimental and numerical study of an elevated pool fire scenario in a confined and mechanically ventilated compartment. Fire Safety Journal, 2024, 142, pp.104046. ⟨10.1016/j.firesaf.2023.104046⟩. ⟨irsn-04588972⟩

HAL Id: irsn-04588972
https://asnr.hal.science/irsn-04588972v1
Submitted on 15 Jan 2025

Experimental and numerical study of an elevated pool fire scenario in a confined and mechanically ventilated compartment

Samuel Vaux[a,*], Emeline Georges[a], Hugues Pretrel[a]

[a]*Institut de Radioprotection et de Sûreté Nucléaire (IRSN), PSN-RES, SA2I, Cadarache, 13115 Saint-Paul-lez-Durance, France*

Abstract

The present work deals with an experimental and numerical investigation of an elevated pool fire scenario in a confined and forced ventilated compartment. Although often encountered in industrial installations or in common buildings, this type of configuration is rarely studied in the literature. This study is supported by a set of two large-scale fire experiments performed in the framework of the OECD-PRISME3 project and numerical simulations (RANS and LES methods) carried out with the CALIF^{3}S-Isis software. The objective is to improve the physical understanding of the phenomena that are experimentally highlighted and to assess the capabilities of Computational Fluid Dynamics (CFD) on this type of configuration. First, the comparison between the two large-scale fire tests (one elevated and its equivalent on the ground) exhibits a strong modification of the fuel mass loss rate associated with a change in the thermal and species stratifications. Then, a preliminary simulation using a predictive approach commonly used and efficient for the case of a ground fire scenario shows by contrast its limitations when applied to the case of the elevated fire. Therefore, in addition to the essential step consisting in the validation of the code with a prescribed approach on this type of elevated fire, the simulations also reveal a specific phenomenology (smoke filling, strong vitiation, oxygen-pumping, ...). Finally, taking into account these particularities allows in fine, for the studied case, the improvement of the prediction of the mass loss rate of the fire.

Keywords: compartment fire, elevated fire, large-scale fire tests, numerical simulations (RANS & LES)

---

[*] Corresponding author

Email address: `samuel.vaux@irsn.fr` (Samuel Vaux)

1. Introduction

Compartment fires represent a key scenario for the fire risk assessment in the industry and in particular in nuclear installations. Actually, the mechanical ventilation of the compartment coupled to the confinement of the gaseous environment around the fire lead to a particular fire scenario. Although this topic has been largely investigated in the literature, the physical phenomena that remain challenging regarding the understanding as well as the prediction with numerical tools are the burning rate and the thermal stratification. During a compartment fire, fuel burning becomes rapidly coupled with the surrounding environment and especially with two antagonist features, the oxygen vitiation and the external heat fluxes. In addition, vertical thermal stratification is also a typical feature of compartment fires and shows particular behavior in case of mechanical ventilation. Because of low ventilation flow rate in comparison to the burning rate, stratification into two homogeneous layers is barely reported in comparison to naturally ventilated enclosures. Compartment fire scenario is mostly depicted with an entire smoke filling; the thermal stratification being characterized with constant vertical gradient.

In this framework, a complex compartment fire scenario is a fire located in the upper part of the room. In this configuration, many questions need to be addressed. How does the fire behave in a highly vitiated and hot upper layer? How is the fire supplied with oxygen? How does the thermal stratification evolve in an elevated fire? In practice, this elevated fire scenario is often identified as, for example, a cable tray fire, located primarily in the upper part of the enclosure. Understanding the dynamics of elevated fires is therefore a major issue in the field of fire safety.

In the past, elevated fire scenarios have been studied, but mainly as a realistic scenario to study other topics of interest, such as fires in mechanically ventilated compartments [1, 2], or to study specific combustion regimes such as ghost flames [3]. Studies focusing specifically on the effect of fire elevation are more recent. The distinguishing feature of these contributions is the ventilation arrangement. The works of Tiwari *et al.*[4], Polukhina [5], Mounaud [6], Coutin *et al.*[7] and Li *et al.*[8] deal with elevated fires in a naturally ventilated compartment. In contrast, Wang *et al.*[9] and Zhang *et al.*[10, 11] focus on a closed compartment. The scenario varies between studies with a gas (propane), heptane, or diesel fire source and compartments of various sizes that are not organized identically, especially for openings in naturally ventilated compartments. Regarding the burning rate, two different conclusions have been reported. Depending on the ventilation configuration, the burning rate can either increase with fire elevation for mechanically ventilated compartments or decrease for naturally ventilated rooms. These two trends illustrate the combined effects of air vitiation, which reduces the power of the elevated fire, and increasing radiative heat fluxes, which, in contrast, promote pyrolysis. It is either the radiative heat fluxes or the oxygen concentration that is predominant and that directs the combustion process. Nevertheless, until now, there is a lack of knowledge to formally explain the coupled effects of these two mechanisms. In addition to the burning rate, some of these studies have also reported a change in vertical stratification due to fire elevation. The filling process and the position of the interface are altered, leading to the identification of the interface under the fire elevation. Given the major issue of correctly predicting thermal stratification in fire risk assessment, it is important to quantify the effect of fire elevation on the thermal stratification.

In order to go further in the understanding of elevated fires, large-scale fire tests have been defined in the OECD-PRISME3 project focusing on a new configuration with a forced ventilated compartment [12]. This scenario is an intermediate between a closed compartment that leads to an increase of the burning rate with elevation and a naturally ventilated compartment that leads to the opposite behavior. The present work proposes an experimental and numerical study of an elevated fire scenario in a forced ventilated compartment. The objective is to better understand the effect of elevation on the burning rate and thermal and species stratifications based on the analysis of large-scale fire tests and CFD numerical simulations. Simulations are also considered here to obtain additional and complementary physical information such as temperature and oxygen concentration fields, too complex to obtain from experiments.

The paper is organized as follows. In §2, the experimental fire test is presented along with the main experimental results. The latter focus on two main points, the experimental evidence of the effect of elevation on the burning rate and thermal stratification in the case of a forced-ventilated enclosure and the effect of fire elevation on the temperature and oxygen concentration fields inside the enclosure. In §3, our numerical model is described and the results of the numerical simulations are presented and compared with the fire tests in §4. Finally, the main conclusions are summarized in §5.

2. Experimental fire test

2.1. Specifications

Large-scale fire tests in forced-ventilated compartment performed in the framework of the OECD PRISME 3 project (test campaign named S3 [12]) are considered. The enclosure, part of the IRSN DIVA facility, consists of three identical rooms (of dimensions length L_x × width L_y × height H=5 m × 6 m × 4 m) connected by doors (of dimensions width×depth×height=0.72 m × 0.3 m × 2.15 m) as illustrated in figure 1. The walls are made of concrete ($\rho = 2700\,\mathrm{kg/m^3}, k = 0.22\,\mathrm{W/K/m}, C_p = 920\,\mathrm{J/kg/K}$) of different thicknesses and the ceiling is made of a multilayer system with concrete (0.3 m), air gap (0.13 m) and a calcium silicate panel of 26 mm thickness ($\rho = 140\,\mathrm{kg/m^3}, k = 0.15\,\mathrm{W/K/m}, C_p = 840\,\mathrm{J/kg/K}$). This three-room assembly was initially configured with the objective of studying multi-compartment scenarios. In this study, dedicated to the effect of fire elevation, the analysis focuses only on the fire room.

The fire source, located in the center of room 3 as shown in figure 1, is a circular pan of surface $S = 0.56\,\mathrm{m^2}$ filled with 56 liters of dodecane fuel ($\Delta H = 42\,\mathrm{MJ/kg}$ and $T_b = 210\,^\circ\mathrm{C}$ with ΔH the combustion enthalpy and T_b the boiling temperature). The fuel was ignited remotely using a 10 kW propane burner. Two elevations are considered at $z_s = 0.36\,\mathrm{m}$ and $z_s = 2.11\,\mathrm{m}$ from ground level (z_s is the vertical position of the bottom of the pan). For the case $z_s = 2.11\,\mathrm{m}$, the pan was positioned on a masonry support made of cellular lightweight concrete blocks.

The ventilation consists of two ventilation lines, an admission line connected in the upper part of the three rooms and an exhaust line connected only in the upper part of the central room. The inlet and outlet sections of these lines are rectangular with dimensions of 0.6 m in height and 0.3 m in width. The direction of the flows is shown in figure 1. These lines are part of an industrial ventilation network equipped with fans. The target ventilation flow rate before ignition was set to $3600\,\mathrm{m^3/h}$ in the exhaust line and equally distributed in the three intake lines at $1200\,\mathrm{m^3/h}$. The target room pressure before ignition was $-80\,\mathrm{Pa}$.

Two tests have been performed, one named PR3_S3_B0 with a fire elevation close to the ground (dimensionless elevation $z_s/H = 0.09$, where H is the height of the room) and the other named PR3_S3_C1 with a higher fire elevation ($z_s/H = 0.55$). The other test parameters are identical for both tests. In addition to these two tests, the fire source was also characterized in open atmosphere under a hood to determine a reference behavior for the burning rate.

Numerous measurements were made during these tests. The present analysis focuses only on the measurements made in the fire room, namely the mass loss rate, gas temperature, species concentration, pressure and flow rate in the ventilation. The measurement positions are shown in figure 1. The fuel mass loss is measured using a SARTORIUS IS300IGG weighing system (full range 300 kg and accuracy of 2 g). The burning rate is deduced from the time derivative of the mass signal. The vertical temperature profiles in the fire room were measured from four vertical masts located symmetrically in the room as indicated in figure 1 and equipped with nine K-type thermocouples of diameter 1.5 mm positioned at 0.05 m, 0.55 m, 1.05 m, 1.55 m, 2.05 m, 2.55 m, 3.05 m, 3.55 m and 3.85 m from the ground. The uncertainty was estimated to be 4 °C for the gas-phase measurements and 16 °C for the flame measurements.

A fifth thermocouple mast was positioned on the pool axis. The vertical temperature profile was also measured at the center of the doorway with seven K-type thermocouples located at 0.1 m, 0.4 m, 0.7 m, 1.4 m, 1.6 m, 1.8 m and 2.0 m from the ground. These measurements were associated with bidirectional velocity probes connected to a pressure transducer to also measure the horizontal velocity profile. The uncertainty in the velocity was estimated to be 5%.

Oxygen, carbon dioxide and carbon monoxide concentrations were measured using gas analyzers (SIEMENS ULTRAMAT 22 for CO_2 and CO and SERVOMEX XANTRA 4100 for O_2) connected to sampling points attached to three locations in the room in the upper part (0.75 m from the ceiling) and lower part (0.9 m from the ground) on the South-West mast as well as near the position of the pool as illustrated in figure 1. Note that the position of the gas measurement in the vicinity of the pool changed between the ground and elevated fire tests. Two sampling points were also added along the vertical axis in the center of the doorway at 0.6 m and 1.6 m from the ground. Gas analyzers measured species concentrations on a dry gas sample. The absolute uncertainty is estimated to be 0.4%vol.

Measurement uncertainties were evaluated from calibration tests, performed before or after the tests, and from data provided by sensor manufacturers. The calibration tests consisted of obtaining the differences between the standard values (from specific calibrated sensors or samples) and the measured values read from the acquisition system. Two levels of uncertainties were defined following the procedure given by Hamins [13]. The standard uncertainties were obtained at room temperature without fire. A second level, the expanded uncertainty, takes into account the fire test conditions and test repeatability, and is introduced by a coverage (or correction) factor, applied to the standard uncertainty.

The test proceeded as follows. First, the ventilation was turned on and the targeted ventilation flow rate was set. The pool was remotely ignited until the fire spreads and stabilises on the pan (with a duration of $\sim 10\,\mathrm{s}$) and then the ignition source was turned off. Then, the combustion progressed until extinction due to the burning of the fuel.

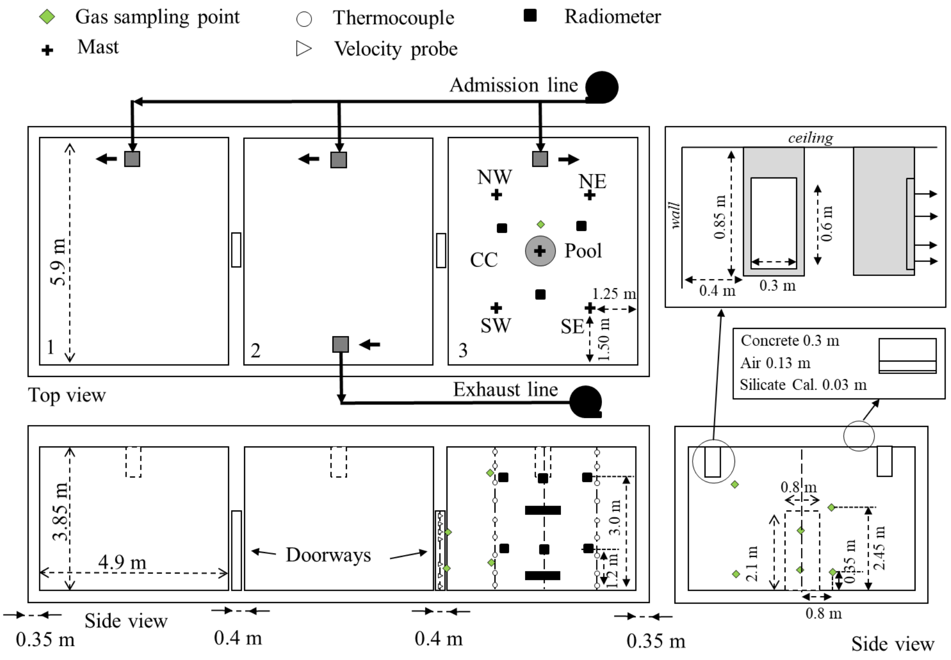

Figure 1: Schematic illustration of the PR3_S3_C1 elevated fire scenario.

2.2. *Experimental results*

The time variation of the mass loss rate (MLR or $\dot{m}$) is significantly influenced by the source elevation. Figure 2a compares the time variation of the MLR for the two pool elevations as well as for the one measured in open atmosphere. The compartment contributes to the reduction of the MLR compared to the open atmosphere behavior. In addition, increasing the fire elevation between $z_s/H = 0.09$ and $z_s/H = 0.55$ also contributes to reducing the MLR. Indeed, a reduction of about 20 % in the value of $\dot{m}$ for the elevated fire during the quasi-stationary phase is observed between these two tests. In this situation, it is actually observed that the fire progressively develops within the hot smoke layer containing the combustion products, thereby reducing de facto the amount of oxygen available. Compared to the open atmosphere test, the reduction in MLR occurs earlier during combustion, especially for the fire elevation $z_s/H = 0.55$. This is due to the air vitiation caused by the smoke filling process in the vicinity of the fire source. The closer the fire is to the ceiling, the earlier the impact on the MLR. A consequence of the reduction in MLR is an increase in fire duration; the initial fuel mass being the same for all three tests. Analysis of the oxygen concentration around the fire confirms the correlation between the decrease in oxygen concentration and the reduction in MLR (see figure 2b).

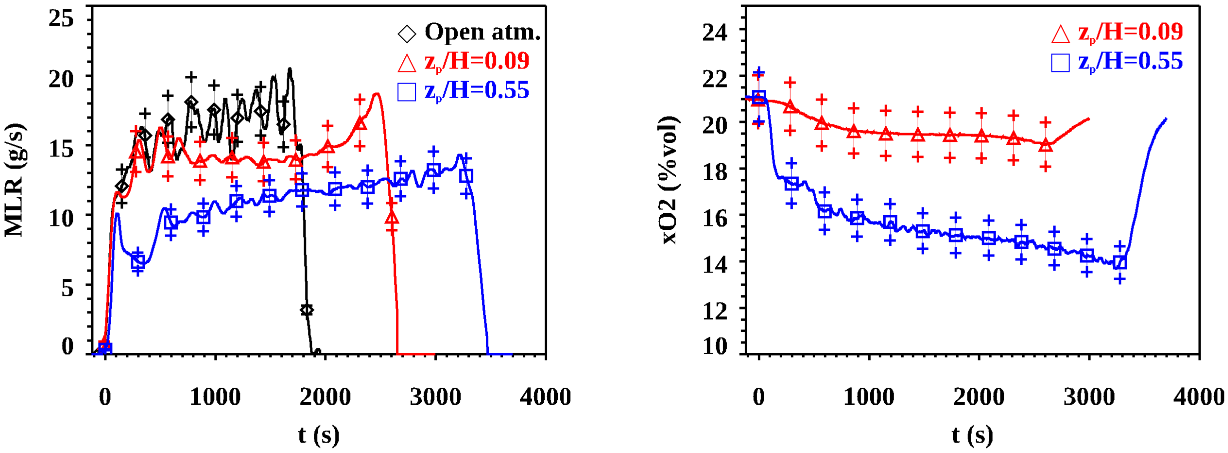

a)

b)

Figure 2: Time variation of a) the burning rate and b) the oxygen concentration near the pool.

The smoke filling process is also influenced by the fire elevation. Figure 3 shows the time variation of species concentration measured in the upper part of the room on the South-West mast (at 0.75 m from the ceiling) for the two fire elevations. The higher fire elevation test leads to a more severely oxygen-depleted smoke layer with higher concentrations of both CO_2 and CO. Increasing elevation de facto reduces the possibility of mixing between the rising fire plume and the entrained air and thus limits the dilution of the smoke layer. The higher the fire elevation, the less diluted the smoke layer becomes. In addition, the time variation of the concentration of CO shows a continuous increase with no steady phase as is the case for the concentration of O_2 and CO_2 or for the MLR. These results show the influence of fire elevation on combustion efficiency. The proximity of the ceiling contributes to the promotion of unburned gas production.

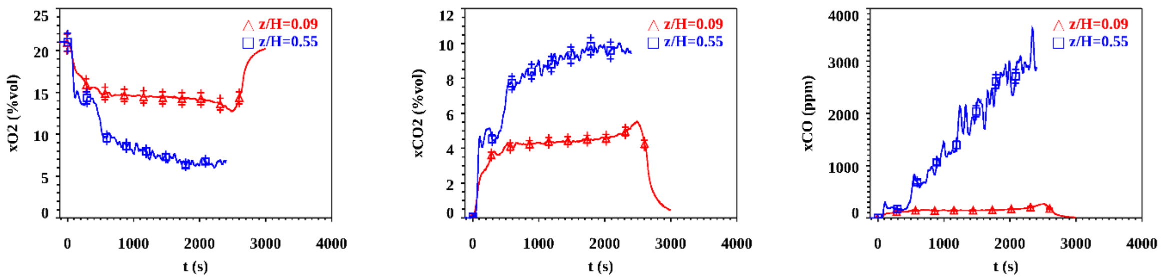

a) b) c)

Figure 3: Time variation of species (O_2, CO_2 and CO) concentrations in the upper part of the room on the South-West mast (the signal for the test $z_s/H = 0.55$ is not displayed after 2400 s because of probe fall from the mast).

In order to study the effect of fire elevation on smoke stratification, the vertical species concentration and temperature profiles, shown in figure 4 at a given time during the steady phase, are also analyzed. The temperature profile is calculated as an average between the four profiles measured with the four masts (NW, NE, SW, and SE as shown in figure 1). The concentration profiles are obtained from a combination of measurements taken at different elevations in the compartment (upper and lower part of the room, fire elevation and top and bottom of the door). The species concentration profiles confirm the change in stratification with elevation. The higher the fire elevation, the thinner and more vitiated the smoke layer. This result is confirmed by the temperature profile which shows a cooler lower zone (below the pool fire, i.e.

for $z < z_s$) and a warmer upper smoke layer (for $z > z_s$).

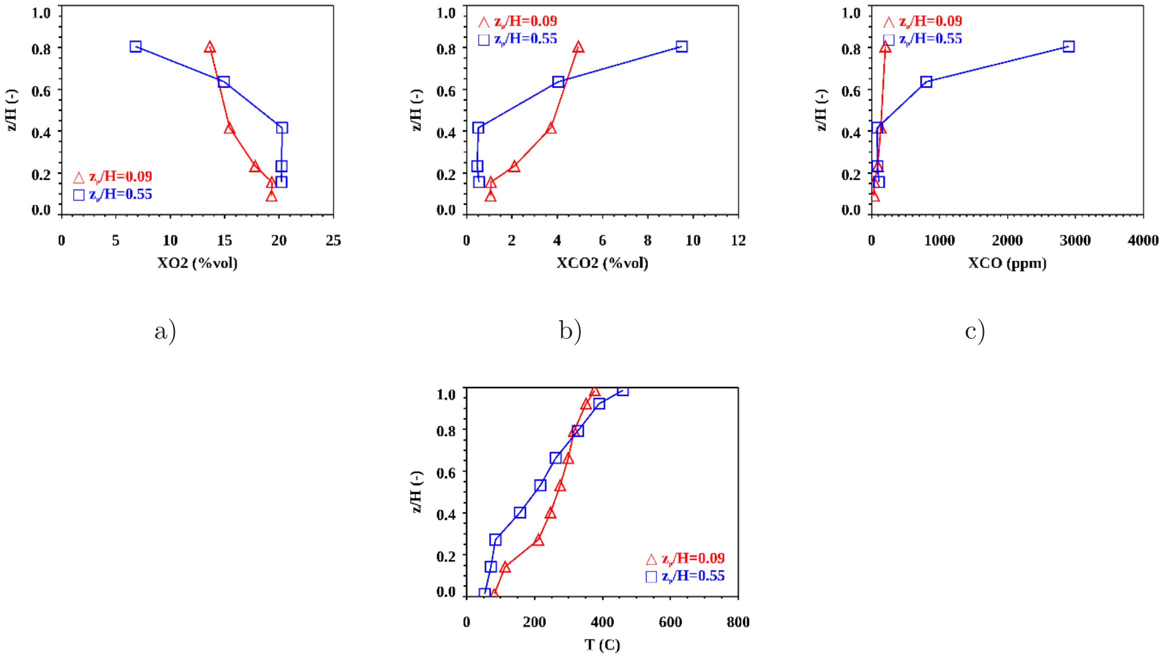

a)

b)

c)

d)

Figure 4: Vertical profiles of a-c) species concentrations (O_2, CO_2 and CO) and d) temperature for the given time $t = 2300\,\mathrm{s}$. The elevations of the measurements for the species concentrations profiles are $(0.35\,\mathrm{m}, 0.6\,\mathrm{m}, 0.9\,\mathrm{m}, 1.6\,\mathrm{m}, 3.10\,\mathrm{m})$ for the ground test and $(0.6\,\mathrm{m}, 0.9\,\mathrm{m}, 1.6\,\mathrm{m}, 2.45\,\mathrm{m}, 3.10\,\mathrm{m})$ for the elevated test.

Finally, in order to take into account the vitiation of the air, it is common to evaluate the mass loss rate $\dot{m}$ as a function of the oxygen concentration X_{O_2} (molar fraction) in the vicinity of the pool fire, ie $\dot{m} = f(X_{\mathrm{O}_2})$. For environments where the oxygen concentration is reduced, a reduction in the mass loss rate is observed. As such, the correlation of Peatross & Beyler [14] (used in particular in the CALIF^{3}S-Isis software for predictive calculations, see §3) expresses in a simple way the effect of air vitiation on the mass loss rate and is written in the following form:

$$\dot{m} = \dot{m}_0(10X_{\mathrm{O}_2} - 1.1), \tag{1}$$

where $\dot{m}_0$ is the mass loss rate in case of fire in normal oxygen concentration (i.e. $X_{\mathrm{O}_2} = 21\%$) and given by the Babrauskas correlation [15]:

$$\dot{m}_0 = S\dot{m}''_\infty(1 - exp(-k\beta D)), \tag{2}$$

where $\dot{m}''_\infty$ is a reference mass loss rate, D is the pool diameter, S the pool area ($S = \pi\, D^2/4$) and $k\beta$ is a fuel constant ($k\beta = 1.8$ m^{-1} in the present case). In (1), X_{O_2} represents the average molar fraction of oxygen in a subdomain Ω close to the flame. In the case of the present tests, when the oxygen sensor in the vicinity of the flame is used, we only mention that the Peatross & Beyler correlation is verified for the experimental ground fire test PR3_S3_B0 but not for the case of the elevated fire test PR3_S3_C1. In fact, we mention that the time-averaged value of the mass loss rate during the steady state of the fire in this case is underestimated by about 40 % by Peatross & Beyler's law.

3. CFD calculation with CALIF^{3}S-Isis

The CALIF^{3}S-Isis[1] software, developed by IRSN, is a computational tool based on low-Mach number approximation dedicated originally to the simulation of fires in mechanically ventilated compartments. This section aims at describing the CFD tool as well as to enumerate several important issues related to the scenario of an elevated fire. Later in the discussion, in §4, the aim will be to evaluate the performance of the CFD tool to simulate the fields of interest (temperature, species concentrations, ...) in comparing the simulations with test results and to bring out phenomena specific to this configuration of elevated fire.

3.1. Physical modelling

The balance equations [16, 17] are written for a weakly compressible flow by using a low-Mach-number approach. In this case, the total pressure P_t is split into three contributions:

$$P_t = P_{\mathrm{th}} + p + \rho_0 g z, \tag{3}$$

where P_{th}, p and $\rho_0\, g\, z$ stand respectively for the thermodynamic, dynamic and hydrostatic pressures. ρ_0 and g represent respectively the ambient density and the gravitational acceleration. P_{th} is constant in space,

---

[1] The CALIF^{3}S-Isis software can be freely downloaded from the following website: https://gforge.irsn.fr/gf/project/isis/.

p depends on both space and time, and the hydrostatic part $\rho_0 g z$ varies only with the height z.

To treat the turbulent nature of the flows encountered in this type of scenario, CALIF^{3}S-Isis allows the use of two different approaches for their simulation. In the first one, a Favre-averaging process is employed to describe the mean scalar and vector fields (e.g. velocity, temperature, composition,...). This averaged process requires closure rules dealt with a turbulence model [18]. The Reynolds-stress tensor and turbulent scalar fluxes are modelled using the eddy viscosity hypothesis and the first-order $k-\epsilon$ model with two balance equations. In the second case, we use large-eddy simulations (LES) in which the transport equations are solved for a filtered velocity field that describes the large-scale turbulent eddies. For these simulations, a box filter in each direction is implicitly applied. The influence of the small-scale turbulent motions is represented by a subfilter model and the WALE (Wall Adapting Local Eddy) subgrid-scale model for the subgrid Reynolds stress [19] is adopted in our simulations.

Standard wall functions are used to take into account the boundary layers near the walls where viscous effects are predominant. Briefly, for the velocity, this near-wall modelling of turbulent flows requires a multi-scale strategy: a model for the boundary layer, generally of analytical type, is derived, and used to obtain boundary conditions for the flow governing equations. A part of the computational domain is dealt with separately, with the above mentioned boundary layer model, then transmission conditions are derived and used as boundary conditions for the actual computation. For the energy balance, the diffusive heat flux is modelled, introducing a convective heat exchange coefficient h_c where h_c can be evaluated using the wall law framework introduced for momentum and turbulent scalar transport equations. A similar log-law layer for temperature is applied near the wall with the introduction of a thermal linear sublayer and a thermal log-law layer for estimating the turbulent heat flux. In the first zone, conductive effects are dominant while in the second, turbulence effects dominate. A more detailed description of the wall laws can be found in [16].

Turbulent combustion is based on the infinitely fast chemistry conserved scalar approach using the mixture fraction and the fuel mass fraction. The mean reaction rate, controlled by the turbulent flow mixing, is determined by the Eddy-Dissipation Combustion (EDC) model [20]. A one-step irreversible combustion reaction for the fuel is considered and involves oxygen and products in the presence of a neutral gas. Among the different approaches available in CALIF^{3}S-Isis to model the soot production and transport, the simplest approach is to consider a coefficient called soot conversion factor, ν_s, in the single one-step reaction [21]. For stoichiometric conditions, the soot conversion factor ν_s is defined as $(Y_s/Y_F)_{st} = \nu_s W_C/\nu_F W_F = y_s$ where Y_F and Y_s are the fuel and soot mass fraction respectively, W_F and W_C are the molar masses of the fuel and carbon species and y_s is a fraction of carbon, originally present in the fuel which is converted to soot during combustion. In the present case, $\nu_s = 1.416$ and we have also carbon monoxide with $\nu_{\mathrm{C}_0} = 0.0546$. The radiative transfers are dealt with the finite volume method [22] assuming a gray and non-scattering medium. The gas absorption coefficient of the mixture used the total emissivity approach of the weighted sum of gray gases model (WSGGM) and the soot absorption coefficient is related to the soot volume fraction according to the Mie theory. The wall conduction is taken into account through the $1D$ Fourier's equation and the convective flux is given by standard laws based on laminar and turbulent Prandtl numbers [23]. The reader can refer to Appendix A of [16] for a detailed presentation of the governing balance equations solved by CALIF^{3}S-Isis software i.e. the Navier-Stokes equations and scalar equations for turbulence (when RANS modelling is applied), chemistry, enthalpy and radiative transfer.

Concerning the boundary conditions, the classical boundary conditions are applied on the walls. Two types of simulation are presented in this article: in prescribed mode (where the experimental mass loss rate (MLR) is imposed as a boundary condition on the fire source area) and in predictive mode. In the prescribed mode, if we assume that what is pyrolysed will burn (a probable assumption for the liquid fuels used in PRISME) then the burning rate is equivalent to the MLR and the reduction in MLR due to air vitiation is already included in the fact that the experimental MLR is imposed as a boundary condition on the pool. So the simulations in prescribed mode presented in this paper were carried out without a flame extinction model. In predictive mode, there are various ways of carrying out simulations. We can use detailed models (pyrolysis, combustion (using a flame extinction model)) or in a more simplified way use a correlation (e.g. of the Peatross & Beyler type). Between these two approaches, it is also possible to use analytical models such as those described in [24, 25]. In the present work, vitiation effects for the fuel vaporisation rate are taken into account by the Peatross & Beyler correlation, without using flame extinction models, which are moreover most often calibrated for ground tests, which is not the case in the present situation.

3.2. Mechanical ventilation modelling

As already mentioned, the thermodynamic pressure P_{th} is constant in space but is a function of time [26]. Indeed, the thermodynamic pressure is expressed through the following overall mass balance equation:

$$\int_{\Omega} \frac{\partial}{\partial t}\left(\frac{P_{\mathrm{th}} W}{\mathcal{R} T}\right) + \sum_{i} Q_i = 0, \tag{4}$$

where Q_i stands for the mass flow rate of the ventilation network at the branch i of the compartment, and the terms W, T and $\mathcal{R}$ represent respectively the molecular weight of the air, the temperature and the universal gas constant. To solve the $i+1$ unknowns, equation (4) is supplemented with a momentum balance equation corresponding to a stationary Bernoulli equation for each branch of the ventilation network:

$$P_t - P_t^{\mathrm{ext,i}} = f \tag{5}$$

where P_t and $P_t^{\mathrm{ext,i}}$ represent respectively the total compartment pressure and the total external pressure at the extremity of the branch i. The head loss f is due to friction and is function of an aeraulic resistance R ($f = sgn(Q_i) R Q_i^2/\rho$).

3.3. CFD issues and challenges in elevated fire scenarios

As mentioned in §2.2, the studied elevated fire test no longer simply fits into the standard framework of tests where the Peatross & Beyler correlation is satisfactory. It is therefore necessary to investigate the reasons for this deviation. To do this, the Computational Fluid Dynamics (CFD) tool is a powerful means of investigation. Indeed, the numerical simulation allows, once the preliminary reproduction of some physical quantities of interest measured experimentally is ensured, to access to local quantities (velocity, temperature, concentrations, ...) on the whole domain and to scrutinize in detail certain physical mechanisms (e.g. aerodynamic, etc.) that large-scale experiments cannot allow.

The purpose of the following CFD calculations is therefore multiple:

- First, a simulation is performed to illustrate that, in contrast with the ground fire, using the CFD code in predictive approach with the Peatross & Beyler law in its standard use [17] leads to an underestimation of the mass loss rate and thus to an erroneous evaluation of the pool fire dynamics. We mention that the terminology 'standard use' refers to the definition of a sub-domain Ω whose reference altitude is taken approximately at the level of the pool fire height z_s and constrained by the presence of walls in ground fires.

- In a second step, since the standard use of the Peatross & Beyler correlation is not valid for the case of the elevated fire under study, we decide to validate the CFD code by simulating only the room of interest, namely the fire room, and thus by imposing the pool mass loss rate $\dot{m}$ as well as the flow at the doorway.
- Once the validation has been carried out, we investigate in more detail the flows specific to this type of elevated fire and discuss the differences with the similar case of a ground fire.
- Finally, based on these observations, we propose an improved predictive model that is integrated into additional simulations. In particular, this allows us to obtain a mass loss rate close ($\sim 10\,\%$) to the one measured experimentally.

4. Numerical results and discussion

4.1. Mesh resolution

Different meshes have been used for the study of the elevated fire scenario. We present in table 1 three meshes, namely M_1, M_2 and M_3 that we have considered the most appropriate for the simulations in the prescribed approach. In the fire room, the number of mesh points in each direction is denoted N_x, N_y and N_z. For the predictive simulations involving the three rooms and as indicated in table 2, we use the mesh M_1 for the fire room and the mesh M_a for the other two rooms (where the number of mesh points in each direction is denoted N_{x_a}, N_{y_a} and N_{z_a}). For each simulation, the total number of cells in the computational domain is denoted N_{tot}. We give a more detailed presentation of the mentioned meshes used for the simulations in appendix A.

	N_x	N_y	N_z	N_{tot}
M_1	47	54	50	$\sim 1.27\ 10^5$
M_2	61	70	61	$\sim 2.62\ 10^5$
M_3	84	103	83	$\sim 7.21\ 10^5$

Table 1: Meshes used for the simulations in prescribed approach (one room)

	N_x	N_y	N_z		N_{x_a}	N_{y_a}	N_{z_a}	N_{tot}
M_1	47	54	50	M_a	35	38	33	$\sim 2.16\ 10^5$

Table 2: Mesh used for the predictive simulations (three rooms)

4.2. Standard predictive simulation

The geometric configuration considered in this preliminary simulation is shown in figure 5 (some parts 265 of the mesh are omitted for the sake of visibility). For the turbulence modelling, we use the RANS method.

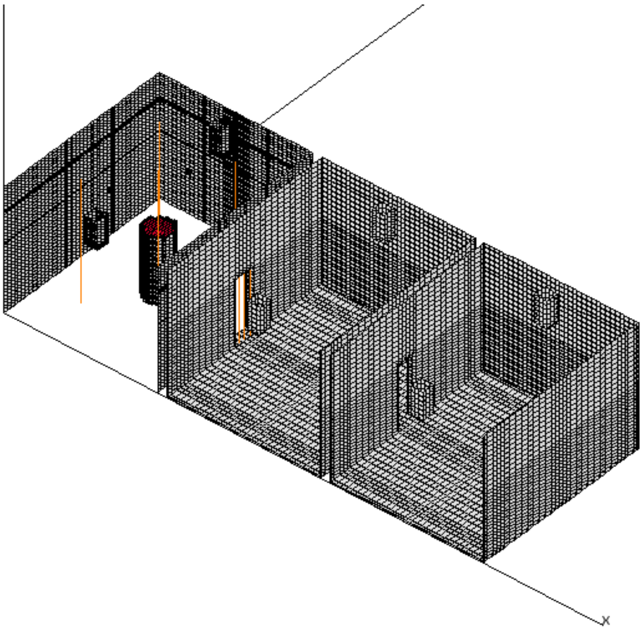

Figure 5: Computational domain used for the configuration of the experimental elevated fire test PR3_S3_C1.

We use the CFD tool in predictive approach, i.e. we prescribe the initial fuel mass and adopt the Peatross

& Beyler correlation to account for air vitiation. This modelling of air vitiation, although simple in its form, has been shown to be valid in many cases of compartment fires. For example, it has been used satisfactorily for pool fires studied in the various and successive PRISME programmes (e.g. PRISME Source [27], Prisme Door [17] and PRISME Integral [27]). For the present elevated fire test case PR3_S3_C1, the mass loss rate given by the simulation is shown in Figure 6a for three simulations $S1$, $S2$ and $S3$. The $S1$ simulation uses a sub-domain of calculation for the averaged value X_{O_2} (involved in the Peatross & Beyler correlation) located on the hollow cylinder $\Omega_1 = \{r \in [r_0 : 2r_0]\} \cup \{z_s < z < z_s + 0.4\,\mathrm{m}\}$ where r_0 is the radius of the pool, r and z are respectively the radial coordinate from the center of the fire source and the vertical coordinate from the ground. In order to identify the possible effect of the size of the sub-domain Ω_i (corresponding to the simulation Si) for the calculation of the averaged value X_{O_2}, the two other simulations $S2$ and $S3$ respectively consider $\Omega_2 = \{r \in [2r_0 : 3r_0]\} \cup \{z_s < z < z_s + 0.4\,\mathrm{m}\}$ and $\Omega_3 = \{r \in [2r_0 : 4r_0]\} \cup \{z_s < z < z_s + 0.4\,\mathrm{m}\}$.

First of all, if we focus on the time interval corresponding to the beginning of the quasi-steady state, i.e. the interval $[500\,\mathrm{s} : 1000\,\mathrm{s}]$, the correspondence between simulation and experiment is correct. Indeed, over this interval, the smoke layer coming from the elevated fire, initially impacting the ceiling and then spreading laterally to participate in the so-called filling-box process, progressively descends to reach the level of the pool fire. The physical phenomenology, at this stage, is close to that encountered in the PRISME Source and Door tests mentioned above. It is illustrated in figure 7a-b where the instantaneous temperature and oxygen concentration fields are respectively represented at $t = 600\,\mathrm{s}$. We also note, as observed in the experiment, that the hot smoke layer remains confined to $z > z_s$ and the severely oxygen-depleted region is restricted to the ceiling region. On this time interval, the standard use of the Peatross & Beyler correlation leads to a correct estimation of the mass loss rate $\dot{m}$.

On the other hand, after this preliminary stage, i.e. for $t > 1000\,\mathrm{s}$, the smoke layer coming from the fire source feeds continuously the space delimited by $z > z_s$ and pollutes this zone continuously. The vitiation of the air is then gradually impacted (and increased) on this zone where the physical phenomenology no longer corresponds to that observed on the time interval $[500\,\mathrm{s} : 1000\,\mathrm{s}]$. In figure 6a, we observe a progressive gap between simulation and experiment in the course of time and conclude that the standard use of the Peatross & Beyler correlation is then taken in default. This remark is valid for the three simulations $S1, S2$ and $S3$ which shows that the radial variation of the size of the subdomain Ω_i weakly modifies the predicted value of the mass loss rate. The difference between simulation and experiment reaches more than 20% over time and could even been expected to be higher if a larger initial fuel mass were considered. Overall, we conclude from this simulation that the experimental mass loss rate is not satisfactorily recovered when using the Peatross & Beyler correlation in the usual way.

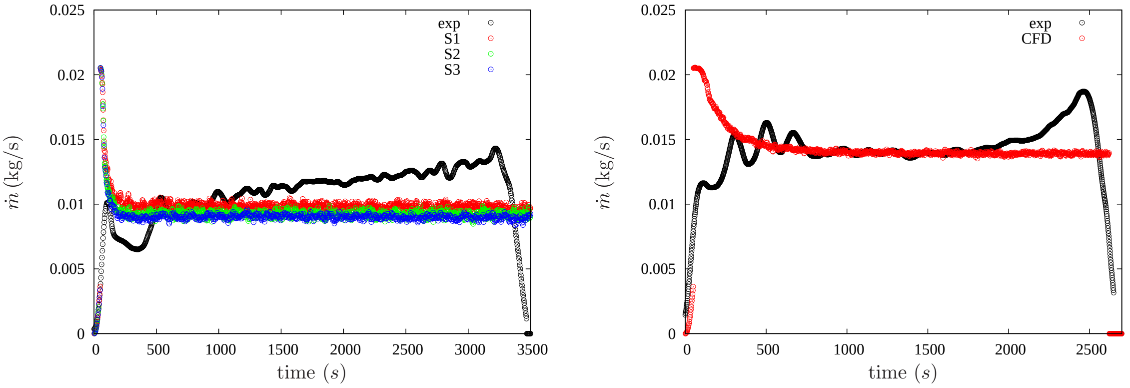

a) elevated fire test (PR3_S3_C1) b) ground fire test (PR3_S3_B0)

Figure 6: Time evolution of the mass loss rate $\dot{m}$ from experiment and predictive simulations a) for the elevated fire test (PR3_S3_C1) b) for the ground fire test (PR3_S3_B0).

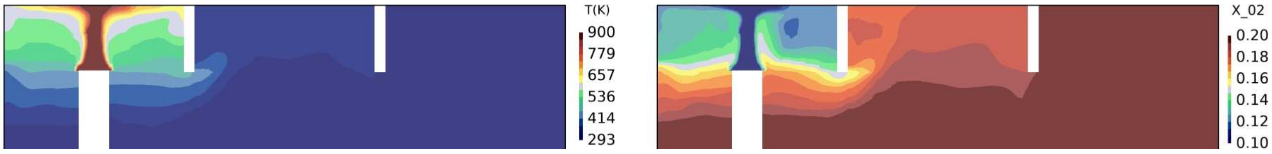

a) $T, t = 600\,\mathrm{s}$ b) $X_{\mathrm{O}_2}, t = 600\,\mathrm{s}$

Figure 7: Temperature T and oxygen molar concentration X_{O_2} fields in the mid-(xz)-plane at the instant $t = 600\,\mathrm{s}$ of the fire scenario - simulation S1.

In addition to the observation of the mass loss rate, it is also interesting to look at the observation of physical quantities that have a specific role in terms of fire safety, namely the relative thermodynamic pressure within the fire room as well as the ventilation rate within the same room. If we now focus only on one simulation, namely $S1$ (we voluntarily discard $S2$ and $S3$ because the conclusions are the same), we can see in figure 8 that these two quantities remain correctly evaluated over time with however an underestimation of the (small) pressure rise over time. The main reason for this acceptable correspondence lies in the low value of the mass loss rate and thus the small power of the fire involved ($\sim 500\,\mathrm{kW}$ during the stationary phase). However, it can be stressed that for higher power fires, as observed for example for cable fires, this correspondence would probably not happen and it would be interesting to focus on the possible occurrence of a reversed flow in the admission duct and thus on the potential negative impact in terms of safety.

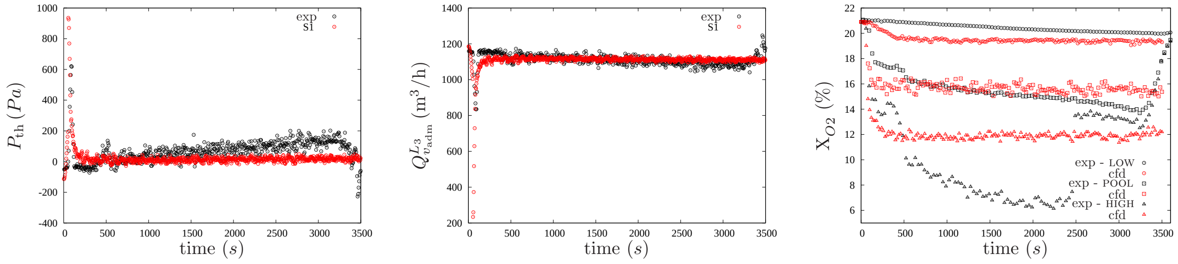

Figure 8: Time evolution of - a) the (relative) atmospheric pressure P_{th}, b) the ventilation volume flow rate (in intake) c) the oxygen molar concentration X_{O_2} at the three experimental points LOW, HIGH et POOL - within the fire room.

Finally, the oxygen concentrations at the three experimental points referenced LOW, HIGH and POOL of coordinates $(3.31\,\mathrm{m}, 4.36\,\mathrm{m}, 0.90\,\mathrm{m})$, $(3.31\,\mathrm{m}, 4.36\,\mathrm{m}, 3.10\,\mathrm{m})$ and $(2.34\,\mathrm{m}, 2.27\,\mathrm{m}, 2.30\,\mathrm{m})$ is represented in figure 8c. The correspondence is correct for the points in the lower part and close to the fire source, but the upper part is much more vitiated experimentally than by simulation.

On this configuration of an elevated fire source, we can then underline the limits of the classical use of Peatross & Beyler's correlation. This limit is further corroborated if we refer to the simulation of the equivalent case with a pool located on the ground (corresponding to the experimental test PR3_S3_B0). For this latter experiment, we represent in figure 6b the mass loss rate $\dot{m}$ obtained by simulation in predictive mode with the common use of the Peatross & Beyler correlation and that obtained experimentally. We note indeed a good agreement between these two quantities on the steady state corresponding to the time interval [350 s : 2000 s].

Thus, in view of these preliminary simulations and in order to try to understand the phenomenology of the elevated fire under study, it seems necessary to reason with a “prescribed approach”, i.e. by imposing the fuel mass loss rate $\dot{m}$ as a boundary condition on the pool. This will allow us first to validate the CFD tool with the experiment on physical quantities of interest and then, once this validation step is obtained, to understand in more detail the underlying physics, or at least to bring some clarifications, on this unique large-scale experimental example.

4.3. Simulations in prescribed approach

In the simulations using a prescribed approach, the experimental fuel mass loss rate is imposed as a boundary condition on the pool. Moreover, as we can guess from figure 7, the flows in the adjacent rooms seem not to constitute zones of strong scientific interest since these rooms act as almost ”dead” zones. Thus, we choose not to simulate them. Therefore, we impose the experimental mass flow rate at the door. To do this, by post-processing the experimental data from the seven velocity and temperature sensors, we are able to create seven geometric zones on the door and impose the experimental mass flow rate on each of them. These zones correspond to the zones of increasing altitude $[0 : 0.25\,\mathrm{m}], [0.25\,\mathrm{m} : 0.55\,\mathrm{m}], [0.55\,\mathrm{m} : 1.05\,\mathrm{m}], [1.05\,\mathrm{m} : 1.5\,\mathrm{m}], [1.5\,\mathrm{m} : 1.7\,\mathrm{m}], [1.7\,\mathrm{m} : 1.9\,\mathrm{m}]$ and $[1.9\,\mathrm{m} : 2.15\,\mathrm{m}]$. In addition, the experimental temperature condition is also imposed on each of these zones. Only the fire room is simulated in the end. In view of this, we have decided to choose mainly a large-eddy simulation (LES) approach in order to capture the physics associated with the elevated fire source in greater detail. We note that, although we have voluntarily reduced the geometrical domain to be simulated (only one room instead of three), the physical time to be simulated remains significant, since it is of the order of one hour. We consider different simulations to evaluate:

- The influence of the mesh size on three successively refined meshes.

- The influence of the combustion chemistry. Indeed, as observed experimentally, the combustion chemistry of dodecane $C_{12}H_{26}$ is somewhat modified for the elevated fire source. It is experimentally observed that the production of carbon monoxide CO is higher (at the expense of soot production) than for the standard confined case.

- the influence of the choice of the turbulence modelling. Indeed, in only one case presented hereafter, we adopt RANS modelling while all the others are carried out using LES.

In what follows, we successively compare the different simulations carried out with the experiment on several physical quantities of interest and also show the results corresponding to the $S1$ simulation in predictive mode.

4.3.1. Thermodynamic pressure and intake ventilation rate

In figure 9a is represented the time evolution of the relative thermodynamic pressure. We note that all the simulations carried out reproduce this quantity in a satisfactory way. As the fire is not very powerful ($\sim 500\,\mathrm{kW}$ in the stationary phase), we cannot expect very high relative pressures. The experiment and the simulations confirm this tendency and we note in particular that the initial pressure peak, of the order of $6\,\mathrm{hPa}$ is correctly reproduced by the simulations. Similarly, at extinction ($t \sim 3400$s), the underpressure peak is very well reproduced by the simulations since it is similarly close to $2.5\,\mathrm{hPa}$. The time evolution of the intake flow rate is represented in figure 9b. Since it is linked to the evolution of the thermodynamic pressure within the fire room, we can see that its reproduction is also very correct for all the simulations. The initial overpressure peak caused by the expansion of the gases due to the initial phase of the fire is followed by a sudden drop in the intake ventilation rate. This drop is correctly represented by the simulations. Subsequently, the quasi-steady state of the fire only slightly changes the experimental ventilation rate, which is also represented by the simulations. At the underpressure peak, the experimental flow rate rises to $1280\,\mathrm{m}^3/\mathrm{h}$ and this rise is accurately reproduced by the simulations.

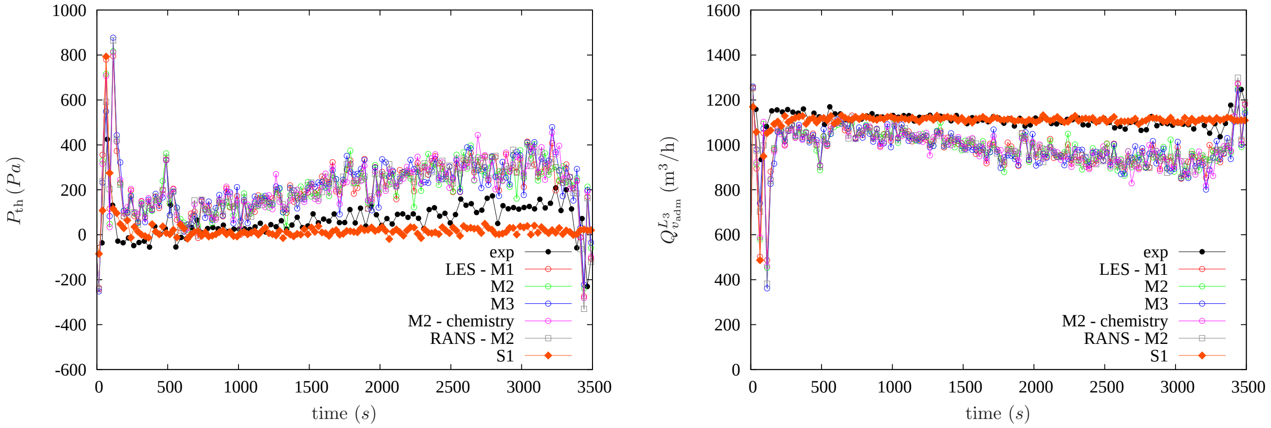

a) relative thermodynamic pressure

b) ventilation (intake)

Figure 9: Time evolution of - a) the (relative) thermodynamic pressure P_{th} and b) the ventilation volume flow rate (in intake) - within the fire room.

4.3.2. Molar species concentrations $\mathrm{O_2}$ *and* $\mathrm{CO_2}$

The time evolution of the oxygen concentration $X_{\mathrm{O_2}}$ is represented respectively in figures 10a-b for the two experimental sensors POOL and HIGH. We note that for the sensor HIGH, the probe fall from the mast at $t \sim 2400\,\mathrm{s}$ explaining the end of the experimental representation at this instant. While on the quasi-steady phase of the fire, $X_{\mathrm{O_2}}$ decreases continuously between 16 % and 14 % in the vicinity of the pool, the numerical simulations follow this trend closely between 16 % and 12.5 %. In the upper part, the correspondence is even better than in the vicinity of the pool since the strong vitiation of the air in the upper part is well reproduced. However, we note that the RANS simulation tends to deviate from the experiment (and also from the other simulations, only LES). On the quasi-stationary plateau, the experiment (as well as the LES) gives $X_{\mathrm{O_2}} \sim 8\,\%$ while the RANS simulation overestimates this value ($\sim 10\,\%$). Moreover, we note that the refinement of the mesh has little influence on the improvement of the calculations, as does the modification of the combustion reaction (modified according to the experimental analysis). It can therefore be emphasised that an LES, even if solved with a relatively coarse grid, gives convincing results (see appendix A for grid sensitivity). The same conclusions can be drawn if we now look at the carbon dioxide concentration, $X_{\mathrm{CO_2}}$, at the two sensors in figure 11. The strong vitiation in the upper part of the room leads to a substantial increase in X_{CO_2} ($\sim 10\,\%$), which is better captured by the LES simulations than by the RANS simulation.

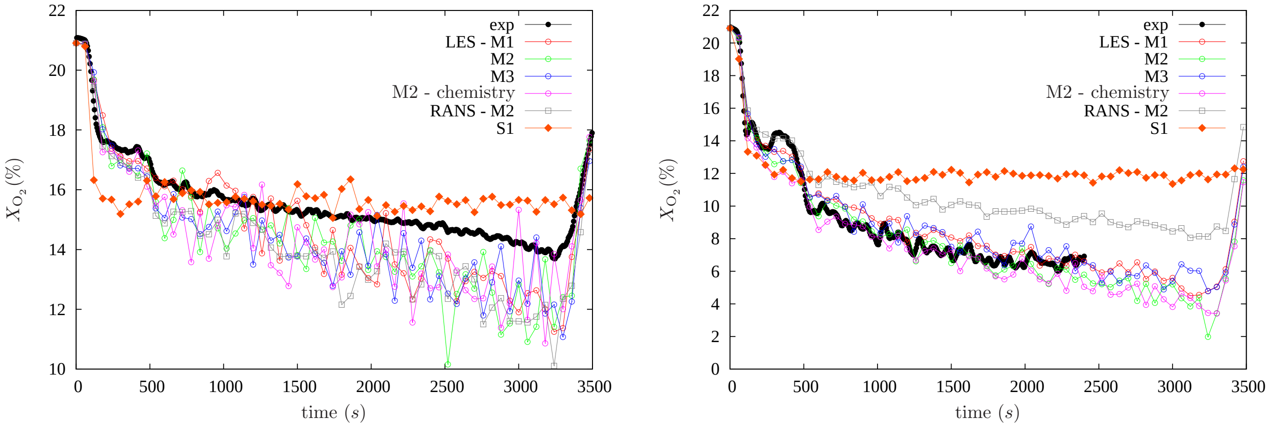

a) pool

b) upper position

Figure 10: Time evolution of the oxygen concentration X_{O_2} a) at the level of the pool (sensor POOL) and b) at the level of the sensor located in the upper part (sensor HIGH) - within the fire room.

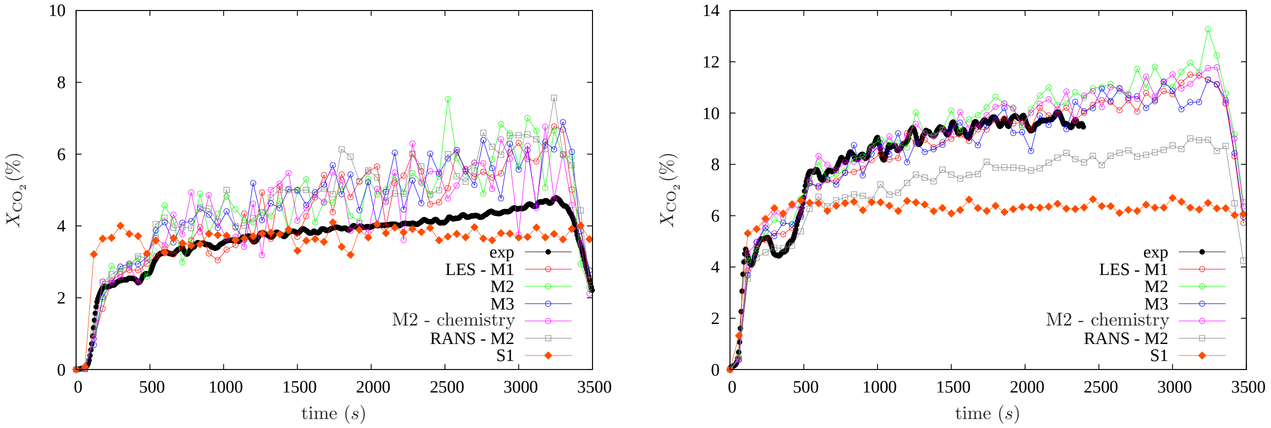

a) pool

b) upper position

Figure 11: Time evolution of the carbon dioxide concentration X_{CO_2} a) at the level of the pool (sensor POOL) and b) at the level of the sensor located in the upper part (sensor HIGH) - within the fire room.

4.3.3. Radiative heat flux on targets

Two radiative heat flux sensors have been installed in the close vicinity of the fire source and are also introduced in our simulations. The measurement of the flux received by these different targets is shown in figure 12 for the two sensors referred as North-East and North-West. On these two sensors, the experimental flux (in the quasi-stationary phase) increases gradually from 6 to $13\,\mathrm{kW/m^2}$ while the simulations evaluate it between 6 to $12\,\mathrm{kW/m^2}$. We note a slight underestimation for the RANS simulation on the North-East and North-West sensors.

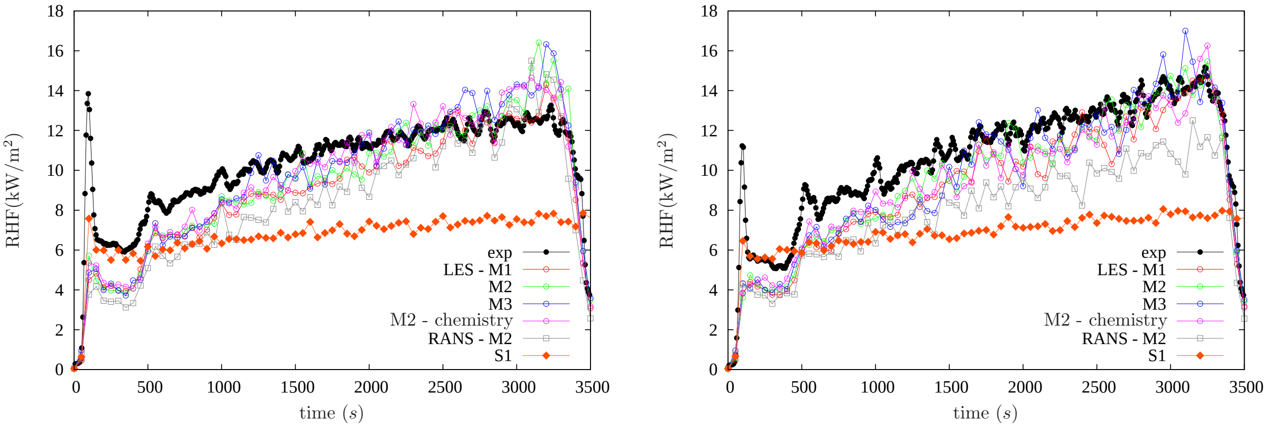

a) North-East sensor

b) North-West sensor

Figure 12: Time evolution of the radiative heat flux on the two sensors North-East and North-West.

4.3.4. Temperature and oxygen fields

We are first interested in the time evolution of the temperature at two points of the South-West thermocouple mast located respectively at a height of 2.05 m and 3.05 m. This evolution is represented in figure 13 for the experiment and the simulations. For the point located at $z = 2.05\,\mathrm{m}$, a maximum difference of the order of $5 - 10\,\mathrm{K}$ is observed, that is to say a relative difference of the order of $1 - 2\%$. The same observation is made for the point located at $z = 3.05\,\mathrm{m}$ with, however, a larger deviation on the time interval $100 - 500\,\mathrm{s}$ and a slight underestimation of the RANS simulation compared to the agreement between the LES simulations and the experiment.

Furthermore, it is also interesting to look at the plot of the vertical temperature profiles for different times. Figure 14 represents these profiles for six different instants, $t = 400, 800, 1200, 1600, 2400$ and $3200\,\mathrm{s}$. Except for the case $t = 400\,\mathrm{s}$ for which an experimental point gives a different value (but moderate, $10\,\%$ of relative deviation) compared to the set of simulations, all the other profiles provide a very good correspondence between simulations and experiment. The RANS simulation is the only one to deviate from the other simulations (LES) and the experiment in the upper part for $z > 3\,\mathrm{m}$.

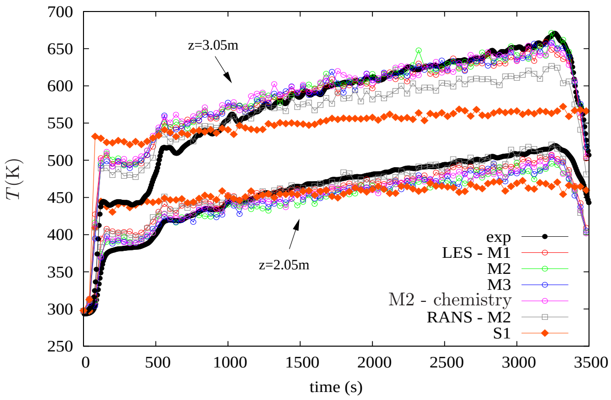

Figure 13: Time evolution of the temperature at two points ($z = 2.05\,\mathrm{m}$ and $z = 3.05\,\mathrm{m}$) on the South-West mast.

The information given by the vertical temperature profiles over time therefore corroborates the experimental observations on thermal stratification. Compared to the equivalent case of the "ground fire" (see figure 4d), the upper smoke layer is warmer while the lower smoke layer is cooler. The smoke filling process in the two cases is different. While in the case of the ground fire, this process takes place over the whole height of the room, it takes place until a level z_f slightly lower than the height of the fire source z_s for the case of the elevated fire. In this last case, the fire continuously supplies the area $z_f < z < H$ with hot smoke, leading to a layer of smoke in the upper part that is hotter than the one in the "ground fire". On the other hand, the lower part, hardly affected by this smoke filling process, has a lower temperature than the "ground fire" case. In terms of fire safety, this suggests that an elevated fire, even if less powerful than its equivalent located on the ground, leads to a higher top layer temperature. Similarly, the temperature under the ceiling is higher which can lead to damage structures (concrete, ...). This constitutes a special vigilance that should be given to this type of fire.

The simulation, once validated with the experiment, gives access to a more global and also more precise vision of this thermal stratification over time. To illustrate this phenomenon in a more exhaustive way, we represent in figure 15 the instantaneous field of temperature T in the median plane (xz) in the course of time. Between $t = 200\,\mathrm{s}$ and $t = 1400\,\mathrm{s}$, we can see that the hot smoke layer in the upper part progressively thickens. Then, we also observe that the layer of hot smoke that is concentrated under the ceiling progressively thickens until the end of the fire. We thus witness a double phenomenon: the progressive development of the hot smoke layer until $z = z_f$ and the accumulation of energy within this layer and more particularly under the ceiling. In figure 16 are represented the average fields of temperature (average carried out on time intervals of duration $\Delta\tau = 200\,\mathrm{s}$) which make it possible to illustrate even more clearly these phenomena by attenuating the local disparities.

Concerning the vitiation of the air, the averaged oxygen concentration fields $\overline{X_{\mathrm{O}_2}}$ are represented in figure 17. It can be seen that the upper part is not strongly vitiated until $t \sim 1000\,\mathrm{s}$. This may partly explain why the preliminary predictive simulation presented a correct estimate of the mass loss rate $\dot{m} = f(t)$ up to this time. From $t = 1400\,\mathrm{s}$, we notice that the upper part is strongly vitiated and this until the fire is extinguished. We notice that the successive layers of oxygen corresponding to increasing oxygen richness (e.g. blue $\overline{X_{\mathrm{O}_2}} \sim 10\%$, green $\overline{X_{\mathrm{O}_2}} \sim 12\%$,...) are not horizontal but have a bell shape. This observation, which is clearly made on the $\overline{X_{\mathrm{O}_2}}$ visualizations, is not shared on the $\overline{T}$ visualizations. It seems therefore that there is a richer oxygen transport coming from the part located under the fire source and feeding the pool fire.

In an attempt to clarify this phenomenology, we represent in figure 18 the mean velocity field as well as the mean oxygen concentration field $\overline{X_{\mathrm{O}_2}}$ in the median plane (yz). For visibility reasons, we voluntarily omit for $z > 2.3\,\mathrm{m}$ the representation of the velocity fields to focus on the lower part of the enclosure. On the zoomed figure 18b, we can see that the oxygen, located in the lower part, is pumped by the pool fire. This phenomenon thus takes part in the deformation of the oxygen layers mentioned before. In view of this mechanism, this leads us to reformulate the predictive simulation by considering an oxygen domain taking into account these observations.

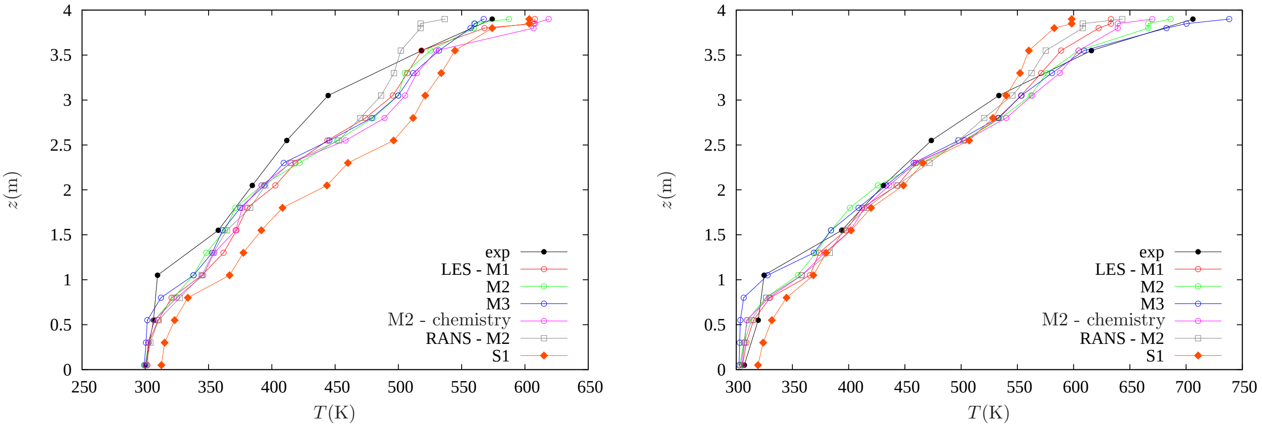

a) $t = 400\,\mathrm{s}$ b) $t = 800\,\mathrm{s}$

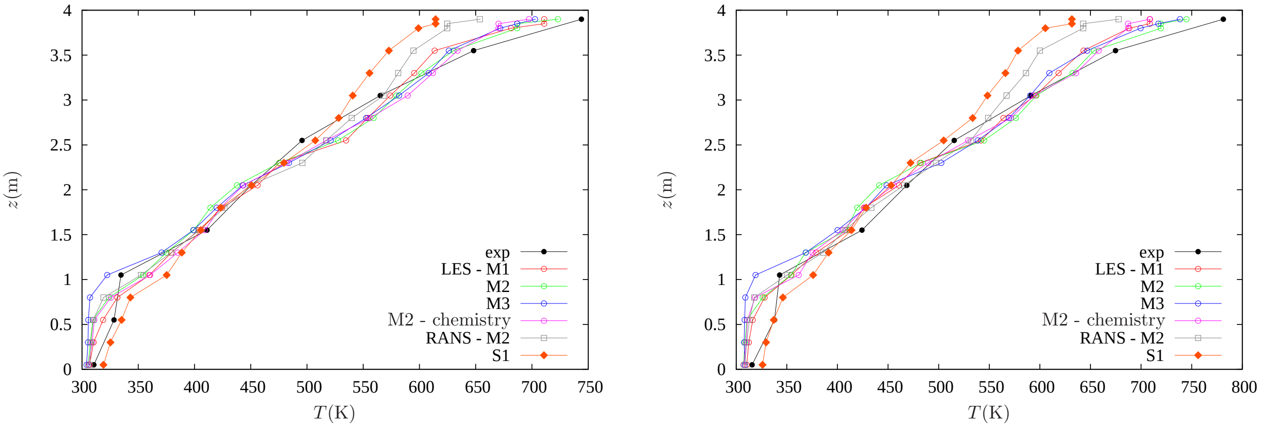

c) $t = 1200\,\mathrm{s}$ d) $t = 1600\,\mathrm{s}$

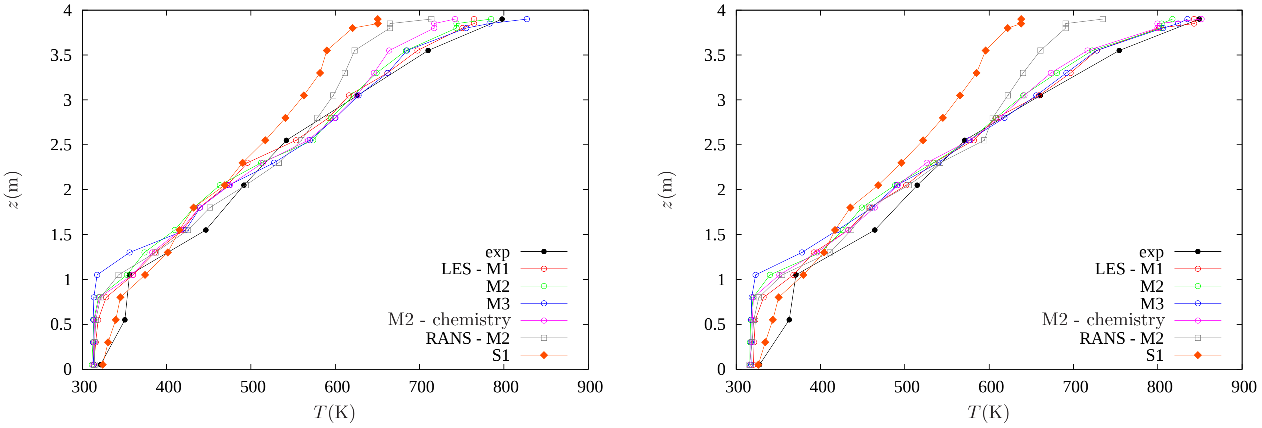

e) $t = 2400\,\mathrm{s}$ f) $t = 3200\,\mathrm{s}$

Figure 14: Temperature profiles on the South-West thermocouple mast for the PR3_S3_C1 test at different times.

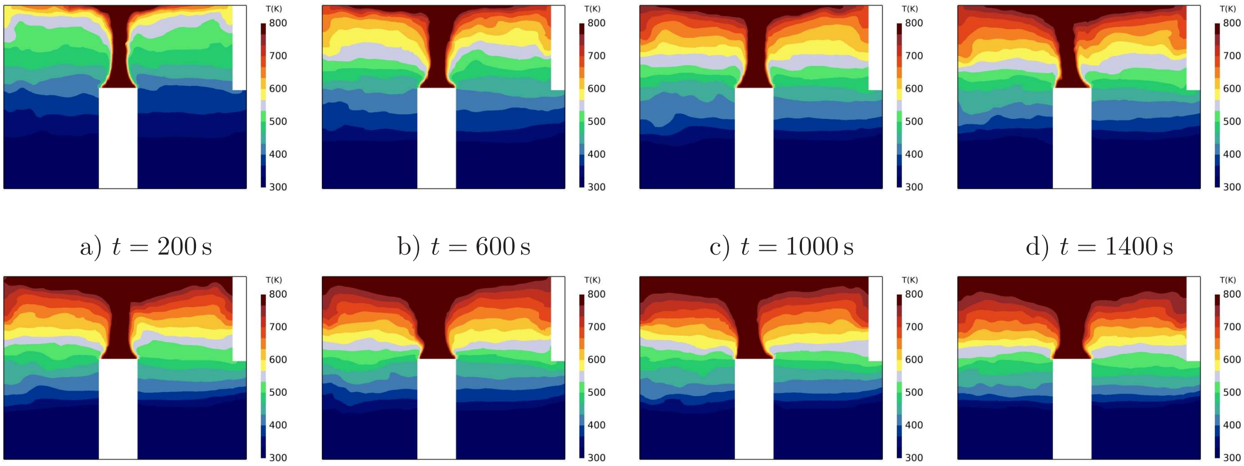

a) $t = 200\,\mathrm{s}$ b) $t = 600\,\mathrm{s}$ c) $t = 1000\,\mathrm{s}$ d) $t = 1400\,\mathrm{s}$

e) $t = 1800\,\mathrm{s}$ f) $t = 2200\,\mathrm{s}$ g) $t = 2600\,\mathrm{s}$ h) $t = 3000\,\mathrm{s}$

Figure 15: Development of the instantaneous temperature field T in the vertical median plane (xz) from $t = 200\,\mathrm{s}$ to $t = 3000\,\mathrm{s}$ with an increment of $\delta t = 400\,\mathrm{s}$ between each snapshot for the elevated fire scenario PR3_S3_C1 - simulation LES - M3.

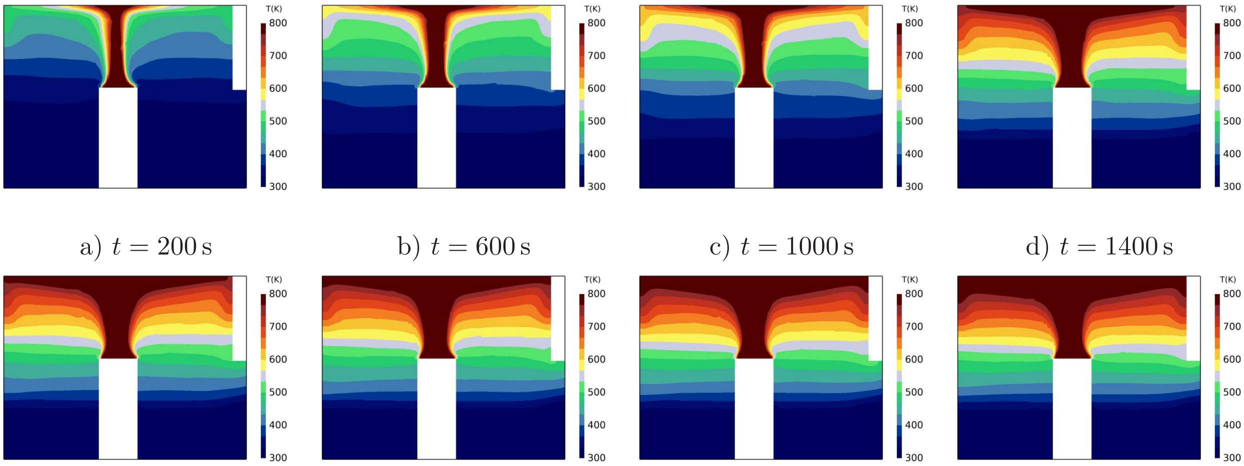

a) $t = 200\,\mathrm{s}$ b) $t = 600\,\mathrm{s}$ c) $t = 1000\,\mathrm{s}$ d) $t = 1400\,\mathrm{s}$

e) $t = 1800\,\mathrm{s}$ f) $t = 2200\,\mathrm{s}$ g) $t = 2600\,\mathrm{s}$ h) $t = 3000\,\mathrm{s}$

Figure 16: Development of the averaged temperature field $\overline{T}$ in the vertical median plane (xz) from $t = 200\,\mathrm{s}$ to $t = 3000\,\mathrm{s}$ with an increment of $\delta t = 400\,\mathrm{s}$ between each snapshot for the elevated fire scenario PR3_S3_C1 - simulation LES - M3.

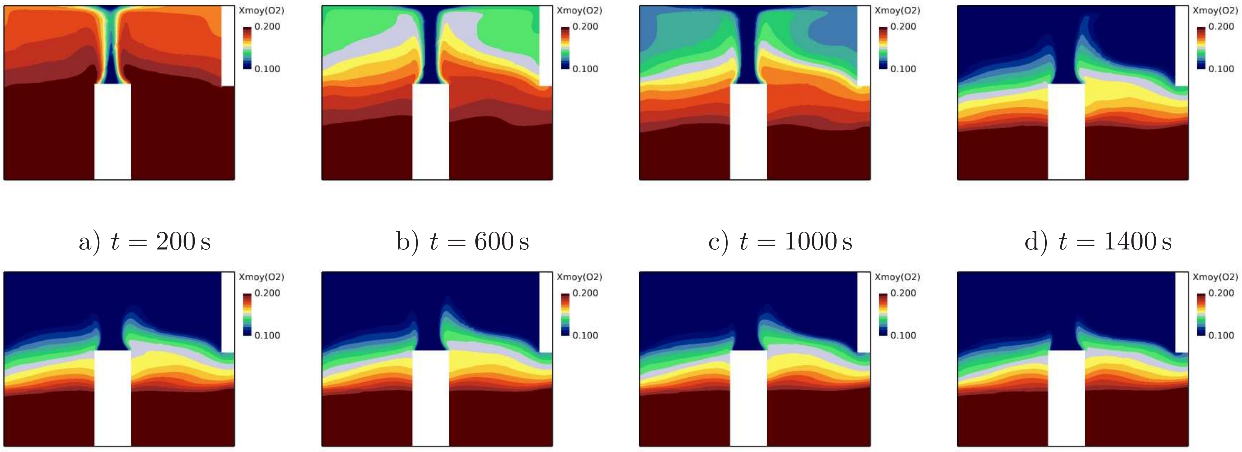

a) $t = 200\,\mathrm{s}$ b) $t = 600\,\mathrm{s}$ c) $t = 1000\,\mathrm{s}$ d) $t = 1400\,\mathrm{s}$

e) $t = 1800\,\mathrm{s}$ f) $t = 2200\,\mathrm{s}$ g) $t = 2600\,\mathrm{s}$ h) $t = 3000\,\mathrm{s}$

Figure 17: Development of the averaged oxygen molar concentration field $\overline{X_{\mathrm{O}_2}}$ in the vertical median plane (xz) from $t = 200\,\mathrm{s}$ to $t = 3000\,\mathrm{s}$ with an increment of $\delta t = 400\,\mathrm{s}$ between each snapshot for the elevated fire scenario PR3_S3_C1 - simulation LES - M3.

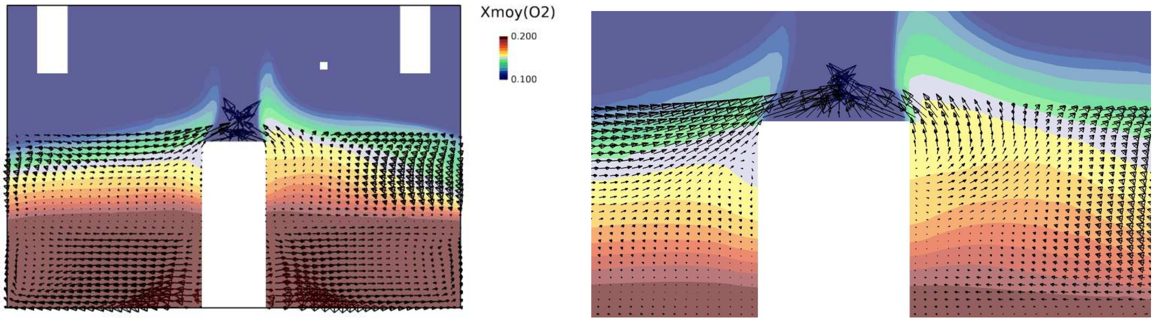

a) in the vertical median plane (yz) b) zoom around the fire source.

Figure 18: Mean velocity field (black arrows) and averaged oxygen molar concentration field $\overline{X_{\mathrm{O}_2}}$ at $t = 2000\,\mathrm{s}$ - a) in the vertical median plane (yz) and - b) zoom around the fire source - simulation LES - M3. Velocity vectors are scaled to give relative velocity magnitude

4.4. Predictive simulations - Suggestions for improvement

The previous observations lead us to reconsider the simulation performed in paragraph 4.2. We now introduce a computational subdomain for the (spatial) averaged value X_{O_2} (involved in the Peatross & Beyler correlation (1)) located on the hollow cylinder $\Omega_1 = \{r \in [r0 : 2r0]\} \cup \{z_s - 0.4\,\mathrm{m} < z < z_s\}$. It can be seen in figure 19 that the mass loss rate now approaches that observed in the experiment. In particular, we can see that the extinction takes place for $t \sim 3400\,\mathrm{s}$, i.e. for a value close ($\sim 5\%$) to the experimental value. In addition to the correction due to this "oxygen-pumping" phenomenon by the fire source, we can also consider an additional correction. Indeed, it has been mentioned that the upper part of the enclosure contains a layer of smoke of high temperature. One can then guess that this smoke layer induces an additional radiation implying a higher mass loss rate due to the additional term $\dot{m}_{\mathrm{add}}$ given by:

$$\dot{m}_{\mathrm{add}} = \sigma(1 - \epsilon_f)(T_g^4 - T_S^4)S/L_{\mathrm{vap}}, \tag{6}$$

where ϵ_f is the flame emissivity, L_{vap} is the vaporization heat, T_S is the fuel surface temperature and T_g is the mean of the gas temperature on the selected region of the smoke layer. In the present case, the flame emissivity as well as the fuel surface temperature are assumed to be constant, respectively $\epsilon_f = 0.92$ and $T_S = 489\,\mathrm{K}$. This simulation is also shown in figure 19 and we can observe that the mass loss rate is increased and close to the experimental one. For the specific case of the test studied (PR3_S3_C1), it seems that the combined effect of the oxygen-pumping by the pool fire associated with the radiation of the smoke layer on the pool participates in the modification of the mass loss rate compared to its equivalent on the ground (PR3_S3_B0 test).

5. Conclusion

Within the framework of the OECD-PRISME3 project, the study of an elevated fire has been considered during the PR3_S3_C1 experimental test. This test, carried out in a confined and mechanically ventilated enclosure, has highlighted significant differences with its equivalent on the ground. These differences are mainly concentrated on the decrease of the mass loss rate, on a strong thermal stratification observed in the

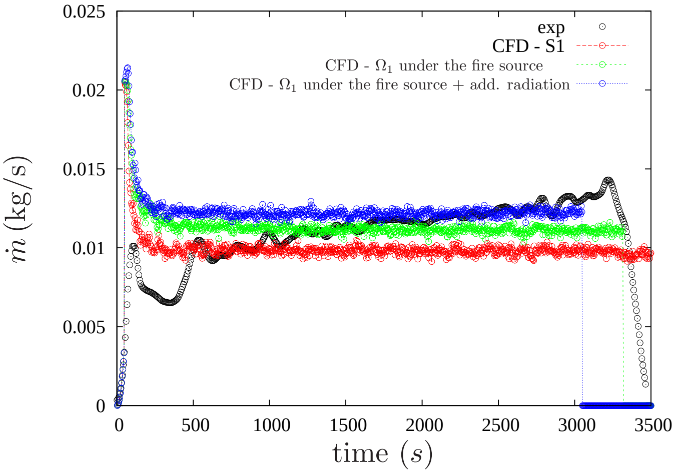

Figure 19: Time evolution of the predicted fuel mass loss rate $\dot{m}$ using a subdomain Ω_1 under the fire source to consider the oxygen-pumping by the pool fire (green curve) and also an additional radiation from the ceiling hot smoke layer (blue curve).

upper part of the compartment combined with a strong vitiation of the air. Based on these experimental observations, the aim of this article was then to study this type of scenario using the CFD tool CALIF^{3}S-Isis. The validation step has been successful since the comparison between physical quantities of interest (temperature, species concentrations, radiative fluxes, ventilation, thermodynamic pressure) is satisfactory between experiment and simulations. Among the different simulations carried out, we note that the LES is the most reliable and that even an LES with a coarse mesh (and thus little cost in computing resources) represents an excellent compromise between quality and computing time. The complementarity between experiments and simulations is revealed in particular by the observation of additional phenomena (oxygen-pumping by the pool fire from below, reinforced radiative effects) by the simulation. Taking into account this particular phenomenology has encouraged us to carry out predictive simulations which are in agreement with the experiment for this kind of scenario. We emphasize that these results could not have been obtained by using the CFD code in a usual way. This unique test represents an important and interesting first step in the study of elevated pool fires and further works will allow us to investigate this type of scenario in greater depth and in particular to refine the first partial conclusions drawn from this large-scale test.

Appendix A. Numerical details

For the mesh M_1, in order to correctly model the fire source, a refined Cartesian grid with a uniform square mesh ($\delta x \times \delta y$) is used over a subregion $R_1 = [L_x/2 - r_0 : L_x/2 + r_0] \times [L_y/2 - r_0 : L_y/2 + r_0]$ centred at the pool fire. To judge the quality of the grid resolution, we consider the characteristic fire diameter D^* defined by $D^* = (\mathrm{HRR}/\rho_\infty c_p T_\infty \sqrt{g})^{2/5}$ where ρ_∞ is the ambient air density, c_p is the air specific heat, T_∞ is the ambient temperature and g is the gravitational constant. A medium resolution can be considered a priori when the grid spacing δx checks $D^*/\delta x \sim 10$. In order to adopt at least a medium resolution, and based on the evaluation of D^* for the elevated fire scenario under study (for which $\mathrm{HRR} \sim 500\,\mathrm{kW}$), we have therefore considered a constant horizontal grid spacing $D^*/\delta x, y \sim 12$ in R_1, corresponding to $\delta x, y/r_0 = 0.15$. In the horizontal x-direction, a subregion R_{2x} surrounds R_1, namely $R_{2x} = [r_0/5 : L_x/2 - r_0] \cup [L_x/2 + r_0 : L_x - r_0/5]$. Over R_{2x}, the horizontal grid spacing is also kept constant, namely $\delta x/r_0 = 0.35$. In the horizontal y-direction, a similar subregion R_{2y} surrounds R_1, namely $R_{2y} = [r_0/5 : L_y/2 - r_0] \cup [L_y/2 + r_0 : L_y - r_0/5]$ with a identical grid spacing, namely $\delta y/r_0 = 0.35$. Finally, close to the walls and outside $R_2 = R_{2x} \times R_{2y}$, the grid is shrinked toward the lateral boundaries of the computational domain. In the vertical z-direction, the grid spacing δz is uniform from the bottom boundary up to a vertical distance $L_{1z} = H - r_0$, and then shrinked toward the upper boundary. The vertical grid spacing was kept constant over L_{1z}, namely $\delta z/r_0 = 0.23$. The choice of the grid spacings $\delta x/r_0$, $\delta y/r_0$ and $\delta z/r_0$ for the mesh M_1 checks for the satisfactory refinement criteria referenced in the papers [28, 29] in which previous simulations compared successfully the LES approach on turbulent miscible Boussinesq and non-Boussinesq flows with experimental data and confirmed the suitability of the CALIF^{3}S-Isis code to properly evaluate the behaviors of turbulent buoyant flows exhibiting large density differences.

The mesh M_2 is obtained from the mesh M_1 by multiplying the grid spacing in each direction by a factor 0.7, leading to about $N_{\mathrm{tot}} = 2.62\,10^5$ cells. The mesh M_3 is similarly obtained from the mesh M_1 by multiplying the grid spacing in each direction by a factor 0.5, leading to about $N_{\mathrm{tot}} = 7.21\,10^5$ cells. Note that for these two refined grids M_2 and M_3, we obtain respectively $D^*/\delta x, y \sim 17$ and $D^*/\delta x, y \sim 24$ over the subregion R_1 covering the fire source. We mention that two subregions have been discretized similarly for the three meshes M_1, M_2 and M_3 : the heat flux sensors with $\delta x/r_0 = \delta y/r_0 = \delta z/r_0 = 0.08$ and the vertical subdomain between the height of the door and the pan height where $\delta z/r_0 = 0.06$.

The meshes (M_1, M_2 and M_3) described above do not include the doorway. However, the flow in the doorway is simulated in all the simulations presented in the paper, both in the predictive and in the prescribed cases. Note that in the latter case, the boundary conditions (mass flow rate and temperature) are applied at the right end (ie $x = L_x + d_\mathrm{d}$, where $d_\mathrm{d} = 0.3\,\mathrm{m}$ is the depth of the door) of the doorway. In the horizontal x-direction, we use a uniform mesh over a subregion $R_\mathrm{door} = [L_x : L_x + d_\mathrm{d}]$ and the value of $\delta x/r_0$ is identical to the horizontal grid spacing used in the subregion R_{2x} of the fire room (respectively $\delta x/r_0 = 0.35$, $\delta x/r_0 = 0.24$ and $\delta x/r_0 = 0.17$ for M_1, M_2 and M_3). In the horizontal y-direction and in the vertical z-direction, the mesh grid is identical to the one used for the fire room.

Considering the mesh used in the two other rooms, in the horizontal x-direction, the grid spacing is kept constant, namely $\delta x/r_0 = 0.35$ (similar to the region R_{2x} of M_1) and is shrinked toward the lateral boundaries of the computational domain. In the horizontal y-direction, the grid spacing is kept constant $\delta y/r_0 = 0.15$ over the width of the door (similar to the grid spacing over the subregion R_1 in M_1) and kept constant, namely $\delta y/r_0 = 0.5$, outside this region and shrinked toward the lateral boundaries of the computational domain. In the vertical direction, the grid spacing is kept constant, namely $\delta z/r_0 = 0.23$ over the height of the door (similar to the vertical grid spacing used for M_1) and kept constant, namely $\delta z/r_0 = 0.6$, outside this region and shrinked toward the lateral boundaries of the computational domain. In addition, to examine the grid sensitivity of the computed solutions, we focus on one specific case, namely the case PR3_S3_C1 simulated in prescribed approach. Among the different time evolutions presented in section 4.3, the grid convergence can be assessed on gas temperature at two points on the South-West thermocouple tree. The results presented in Figure 13 do not show differences greater than $5 - 10\,K$ in the hot upper layer (corresponding to a relative difference of the order of $1 - 2\%$). This is considered as satisfactory for simulations of real large-scale fire scenario and confirms the relevance of the grid resolution based on the characteristic fire diameter D^* mentioned above. Furthermore, we refer the reader to the works [26, 30] for the sensitivity analysis and the validation of the CALIF^{3}S-Isis code.

[1] J. Backovsky, K. Foote, N. Alvares, Temperature profiles in forced-ventilation enclosure fires, Fire Saf. Sci. 2 (1989) 315–324.

[2] B. Cetegen, Entrainment and flame geometry of fire plumes, Ph.D. thesis, California Institute of Technology (1982).

[3] O. Sugawa, K. Kawagoe, Y. Oka, I. Ogahara, Burning behavior in a poorly-ventilated compartment fire-ghosting fire, Fire Science Technology 9 (1989) 5–14.

[4] M. Tiwari, A. Gupta, R. Kumar, P. Sharma, Effects of elevated pool fire in a naturally ventilated compartment, J. Therm. Anal. Calorim. 146 (2021) 341–353.

[5] K. Polukhina, Elevated fires, Master's thesis, Lund University - Division of Fire Safety Engineering (2016).

[6] L. Mounaud, A parametric study of the effect of fire source elevation in a compartment, Master's thesis, Virginia Polytechnic Institute and State University, Virginia (2004).

[7] M. Coutin, B. Gautier, J. Most, Behavior of the combustion of a fuel material in the vitiated upper zone of an open compartment, in: 3rd Int. Semin. Fire Explos. Hazards, 2000.

[8] Z. Li, Y. Zhang, H. Guo, Y. Lin, Y. Cheng, Y. Gao, L. Chen, X. Li, S. Xing, T. Li, Experimental study on the influence of fire source elevation on smoke temperature profile driven by buoyancy in a full-scale mountain tunnel, Combust. Sci. and Technol. 0 (0) (2021) 1–18.

[9] J. Wang, S. Lu, Y. Hu, H. Zhang, S. Lo, Early stage of elevated fires in an aircraft cargo compartment: A full scale experimental investigation, Fire Technol. 51 (2015) 1129–1147.

[10] J. Zhang, S. Lu, Q. Li, R. Kwok Kit Yuen, B. Chen, M. Yuan, C. Li, Smoke filling in closed compartments with elevated fire sources, Fire Saf. J. 54 (2012) 14–23.

[11] J. Zhang, S. Lu, Q. Li, R. Yuen, M. Yuan, C. Li, Impacts of elevation on pool fire behavior in a closed compartment: A study based upon a distinct stratification phenomenon, J. Fire Sci. 31 (2) (2013) 178–193.

[12] S. Suard, P. Zavaleta, H. Pretrel, Overview of the OECD Prisme 3 project, in: Proceedings of SMiRT 25, 2019, Ottawa, ONT, Canada.

[13] A. Hamins, K. McGrattan, Verification and validation of selected fire models for nuclear power plant applications. Volume 2. Experimental uncertainty (NUREG 1824) (2007-05-01 2007).

[14] M. Peatross, C. Beyler, Ventilation effects on compartment fire characterization, in: I. A. for Fire Saf. Sci. (Ed.), International Symposium of Fire Safety Science, Vol. 5, 1997, pp. 403–414.

[15] V. Babrauskas, Estimating large pool fire burning rates, Fire Technol. 19 (1983) 251–261.

[16] ISIS 6.0.0.: Physical Modelling. Institut de Radioprotection et de Sûreté Nucléaire, https://gforge.irsn.fr/gf/project/isis/.

[17] S. Suard, S. Vaux, M. Forestier, Toward predictive simulations of pool fires in mechanically ventilated compartments, Fire Saf. J. 61 (2012) 54–64.

[18] V. Novozhilov, Computational fluid dynamics modeling of compartment fires, Prog. Energy Combust. Sci. 27 (6) (2001) 661–666.

[19] F. Nicoud, F. Ducros, Subgrid-scale stress modelling based on the square of the velocity gradient tensor, Flow, Turbul. Combust. 62 (3) (1999) 183–200.

[20] B. Magnussen, B. Hjertager, On mathematical modeling of turbulent combustion with special emphasis on soot formation and combustion, in: Symposium International on Combustion, Vol. 16, 1976, pp. 719–729.

[21] V. Novozhilov, H. Koseki, Cfd prediction of pool fire burning rates and flame feedback, Combust. Sci. Technol. 176 (2004) 1283–1307.

[22] J. Chai, H. Lee, S. Patankar, Finite volume method for radiation heat transfer, J. of Thermophysics and Heat Transfer 8 (1994) 419–425.

[23] G. Cox, Combustion fundamentals of fire, Academic Press, 1995.

[24] S. Suard, A. Nasr, S. Melis, J. Garo, H. El-Rabii, L. Gay, L. Rigollet, L. Audouin, Analytical approach for predicting effects of vitiated air on the mass loss rate of large pool fire in confined compartments, Fire Saf. Sci. 10 (2011) 1513–1524.

[25] A. Nasr, S. Suard, H. El-Rabii, L. Gay, J. Garo, Fuel mass-loss rate determination in a confined and mechanically ventilated compartment fire using a global approach, Combust. Sci. Technol. 183 (12) (2011) 1342–1359.

[26] S. Suard, C. Lapuerta, A. Kaiss, B. Porterie, Sensitivity analysis of a fire field model in the case of a large-scale compartment fire scenario, Num. Heat Trans., Part A 63 (2013) 879–905.

[27] I. Development Team, ISIS v6 : Validation, Rapport Technique RAPPORT IRSN 2021-235, SA2I/LIE (mar 2021).

[28] R. Mehaddi, S. Vaux, F. Candelier, O. Vauquelin, On the modelling of steady turbulent fountains, Environmental Fluid Mechanics 15 (6) (2015) 1115–1134.

[29] S. Vaux, R. Mehaddi, O. Vauquelin, F. Candelier, Upward versus downward non-Boussinesq turbulent fountains, Journal of Fluid Mechanics 867 (2019) 374–391.

[30] S. Suard, A. Koched, H. Pretrel, L. Audouin, Numerical simulations of fire-induced doorway flows in a small scale enclosure, Int J Heat Mass Trans. 81 (2015) 578–590.